Magnetic properties and intrinsic ferromagnetism in (Ga,Fe)Sb ferromagnetic semiconductors

Nguyen Thanh Tu,[1] Pham Nam Hai,[1,2] Le Duc Anh,[1] and Masaaki Tanaka[1]
[1]*Department of Electrical Engineering & Information Systems, The University of Tokyo, 7-3-1 Hongo, Bunkyo, Tokyo 113-8656, Japan*
[2]*Department of Physical Electronics, Tokyo Institute of Technology, 2-12-1 Ookayama, Meguro, Tokyo 152-0033, Japan*

(Received 13 July 2015; revised manuscript received 4 September 2015; published 2 October 2015)

We systematically investigate the crystal structure, magneto-optical properties, magnetization, and magnetotransport properties of a new ferromagnetic semiconductor $(\mathrm{Ga}_{1-x},\mathrm{Fe}_x)\mathrm{Sb}$ grown by low-temperature molecular beam epitaxy. Crystal structure analyses by x-ray diffraction, scanning transmission microscopy, and transmission electron diffraction indicate that the $(\mathrm{Ga}_{1-x},\mathrm{Fe}_x)\mathrm{Sb}$ thin films maintain the zinc-blende crystal structure up to $x = 20\%$. We carried out the characterizations of the magnetic properties of the $(\mathrm{Ga}_{1-x},\mathrm{Fe}_x)\mathrm{Sb}$ thin films by various methods, including magnetic circular dichroism spectroscopy, anomalous Hall effect, and superconducting quantum interference device magnetometry, and found that (Ga,Fe)Sb is an intrinsic ferromagnetic semiconductor without any second-phase precipitations. The Curie temperature T_C of $(\mathrm{Ga}_{1-x},\mathrm{Fe}_x)\mathrm{Sb}$ depends on x and hole concentration, as in the case of hole-induced ferromagnetism. The highest T_C reaches 230 K at $x = 20\%$, which is the highest value so far reported in III-V based ferromagnetic semiconductors.

DOI: 10.1103/PhysRevB.92.144403 PACS number(s): 85.75.−d, 73.61.Ey

I. INTRODUCTION

Development of new ferromagnetic semiconductors (FMSs) is an important issue in the emerging field of semiconductor spintronics. In FMSs, nonmagnetic atoms of the host semiconductors are partly replaced by magnetic atoms, which have local magnetic moments. Ferromagnetic coupling between local magnetic moments induces macroscopic ferromagnetism in the host semiconductors, while other important features of the host semiconductors are preserved [1–3]. The band structure of FMSs shows spin splitting due to s,p-d exchange interactions between the local magnetic atoms and the host atoms. This feature is one of the most important characteristics of *intrinsic* FMSs, differentiating them from nonmagnetic semiconductors containing embedded ferromagnetic precipitations. In intrinsic FMSs, one can utilize the spin degree of freedom to design new devices with very attractive functions that are not available using conventional semiconductors, such as spin diodes [4] and spin transistors [5,6] that have spin-dependent output characteristics. Spin transistors are expected to be used as the basic element of low-power-consumption, nonvolatile, and reconfigurable logic circuits [7]. For the past two decades, most of the studies on FMS have been concentrated on Mn-doped III-V p-type FMSs, such as (In,Mn)As and (Ga,Mn)As, which show hole-induced ferromagnetism [8–11]. The Curie temperature T_C of such hole-induced FMSs depends on the Mn concentration x and the hole concentration p. Therefore, many ferromagnetic properties, such as T_C or magnetic anisotropy, can be controlled by changing the Mn doping concentration and/or the hole concentration using electrical gating [12] and light irradiation [9]. Such new functionalities have made the Mn-based FMSs, in particular GaMnAs, standard materials for exploring many novel features of FMSs.

However, Mn-based FMSs have the following unsolved problems from both practical and physical points of view. First, it is impossible to fabricate n-type Mn-based FMSs because Mn atoms are acceptors in III-V semiconductors. Second, the maximum Curie temperature T_C of (Ga,Mn)As (200 K) and (In,Mn)As (90 K) reported so far are still much lower than room temperature despite their very high hole concentrations ($10^{20} - 10^{21}\ \mathrm{cm}^{-3}$) [13,14]. Third, there has been a dispute on the band structure and the origin of ferromagnetism. The mean-field Zener model argues that the Fermi level is located in the valence band and that the ferromagnetism is governed by the p-d exchange interactions between valence-band holes and localized Mn d electrons [15,16]. In contrast, many recent experiments have shown that the Fermi level of the Mn-based FMSs resides in an impurity band [17–20], questioning the validity of the valence-band Zener model. Recently, in order to overcome those shortcomings of the Mn-based FMSs, we have proposed and prepared a new family of FMSs based on Fe-doped narrow-gap III-V semiconductors. Since Fe atoms are isoelectronic when doped in III-V (i.e., they are neither acceptors nor donors), we can control the Fe concentration, carrier-type, and carrier concentration independently. This means one can fabricate both n-type and p-type Fe-based FMSs, which are indispensable for realizing realistic spin devices such as spin diodes and spin transistors. Indeed, we have successfully grown the first n-type FMS (In,Fe)As by low-temperature molecular beam epitaxy (LT-MBE) [21–23]. (In,Fe)As exhibits surprisingly large s-d exchange interaction (2.8 eV for thick films [22] and 4.5 eV for quantum wells [24]), which is significantly larger than the p-d exchange interaction reported in II-VI and III-V FMSs such as (Zn,Mn)Te (−1.1 eV) [25] and (Ga,Mn)As (−1.2 eV) [26]; their T_C can be several tens of Kelvin even when the electron concentration n is as low as $10^{18} - 10^{19}\ \mathrm{cm}^{-3}$. Furthermore, very recently, we have successfully grown a new p-type Fe-based FMS (Ga,Fe)Sb. Notably, T_C of $(\mathrm{Ga}_{1-x},\mathrm{Fe}_x)\mathrm{Sb}$ reaches 140 K at $x = 13.7\%$, which is the highest T_C in narrow-gap III-V FMSs [27]. The successful growth of n-type (In,Fe)As and p-type (Ga,Fe)Sb FMSs opens a new opportunity to fabricate all-FMS spintronic devices.

In this paper, we systematically investigate the crystal structure, magneto-optical properties, magnetization, and magnetotransport properties of $(\mathrm{Ga}_{1-x},\mathrm{Fe}_x)\mathrm{Sb}$ with Fe concentration up to $x = 20\%$. The crystal structure was carefully investigated

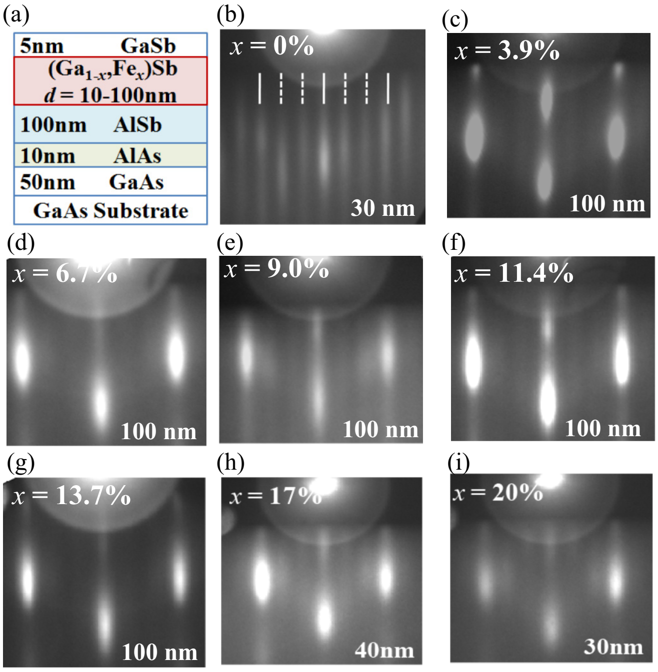

FIG. 1. (Color online) (a) Schematic sample structure studied in this paper. (c)–(i) RHEED patterns taken along the $[\bar{1}10]$ azimuth after the MBE growth of the $(Ga_{1-x},Fe_x)Sb$ layers for samples A–G ($x = 3.9 - 20\%$, thickness $d = 30 - 100$ nm). The RHEED pattern of an undoped GaSb sample is also shown as a reference in (b).

by x-ray diffraction (XRD), scanning transmission electron microscopy (STEM), and transmission electron diffraction (TED). We show that $(Ga_{1-x},Fe_x)Sb$ maintains the zinc-blende crystal structure up to $x = 20\%$. The intrinsic ferromagnetism is confirmed by various characterization methods including magnetic circular dichroism (MCD) spectroscopy, anomalous Hall effect (AHE) measurements, and superconducting quantum interference device (SQUID) magnetometry. The highest T_C observed in (Ga,Fe)Sb reaches 230 K for the sample with $x = 20\%$, which surpasses the highest T_C ($\sim$200 K) of (Ga,Mn)As. Our results indicate that the Fe-based FMSs are among the best candidates for post-(Ga,Mn)As materials for semiconductor spintronics and are very promising for realization of high-T_C FMSs.

II. EXPERIMENTS

The studied $(Ga_{1-x},Fe_x)Sb$ layers were grown on semi-insulating GaAs(001) substrates by LT-MBE. The schematic structure of our samples is shown in Fig. 1(a). After growing a 50-nm-thick GaAs buffer layer at 550 °C, we grew a 10-nm-thick AlAs layer at the same substrate temperature. Then, we grew a 100-nm-thick AlSb at 470 °C. At this stage, the lattice mismatch between (Ga,Fe)Sb (which is very close to the lattice constant of GaSb, $a_{\mathrm{GaSb}} = 0.609$ nm) and GaAs ($a_{\mathrm{GaAs}} = 0.565$ nm) is relaxed, and a very smooth AlSb surface was obtained. After that a $(Ga_{1-x},Fe_x)Sb$ layer with various Fe concentrations ($x = 3.9 - 20\%$) and thicknesses ($d = 10 - 100$ nm) was grown at a typical growth rate of 0.5 µm/h at 250 °C. Finally, a 5-nm-thick GaSb cap layer was grown to prevent oxidation of the underlying (Ga,Fe)Sb layer. The Fe flux was calibrated by secondary ion mass spectroscopy and Rutherford back scattering. The studied $(Ga_{1-x},Fe_x)Sb$ samples are listed in Table I. First, we examined samples A–E with various Fe concentrations $x = 3.9 - 13.7\%$ and a fixed thickness $d = 100$ nm. Then, we investigated samples $F_1 - F_5$ with a fixed Fe concentration $x = 17\%$ and reduced thicknesses $d = 10$–50 nm to study the thickness dependence of the magnetic properties. Finally, we investigated a 30-nm-thick $(Ga_{1-x},Fe_x)Sb$ with $x = 20\%$ (sample G) to study the magnetic properties of this heavily Fe-doped sample.

During the MBE growth, reflection high-energy electron diffraction (RHEED) was used to observe the crystallinity and surface morphology of the samples. XRD was used to determine the lattice constant of the epitaxial (Ga,Fe)Sb layers. STEM and TED were employed to characterize the crystal structure of the (Ga,Fe)Sb layers. The magneto-optical properties of the (Ga,Fe)Sb layers were characterized by MCD spectroscopy and its magnetic field dependence. The magnetization of the (Ga,Fe)Sb layers were measured by SQUID. The magneto-transport measurements of the (Ga,Fe)Sb layers were carried out by using Hall bars with a size of 200 μm × 50 μm.

III. RESULT

A. Crystal structure analysis

Figures 1(c)–1(i) show the RHEED patterns taken along the $[\bar{1}10]$ azimuth of series A–G of $(Ga_{1-x},Fe_x)Sb$ ($x = 3.9 - 20\%$) after the MBE growth of the (Ga,Fe)Sb layers. For a

TABLE I. Thickness d, Curie temperature T_C, resistivity ρ, hole concentration p at 300 K, p-d exchange interaction $N_0\beta$, and saturation magnetization M_S of $(Ga_{1-x},Fe_x)Sb$ samples A–G with various Fe concentrations $x = 3.9 - 20\%$ and layer thicknesses $d = 10 - 100$ nm.

Sample	x(%)	d (nm)	T_C (K)	ρ(Ω cm)	p (cm^{-3})	$N_0\beta$ (eV)	M_S (μ_B/Fe atom)
A	3.9	100	20	1.0×10^{-1}	4.4×10^{18}	1.96	–
B	6.7	100	27	7.9×10^{-2}	7.8×10^{18}	1.58	–
C	9.0	100	50	6.6×10^{-2}	1.3×10^{19}	1.70	–
D	11.4	100	80	4.7×10^{-2}	4.0×10^{19}	1.59	2.4
E	13.7	100	140	3.1×10^{-2}	4.6×10^{19}	1.87	2.6
F_1	17.0	50	180	–	–	–	–
F_2	17.0	40	180	5.6×10^{-2}	–	–	2.8
F_3	17.0	30	175	–	–	–	–
F_4	17.0	20	160	–	–	–	–
F_5	17.0	10	150	–	–	–	–
G	20.0	30	230	6.6×10^{-2}	–	–	2.9

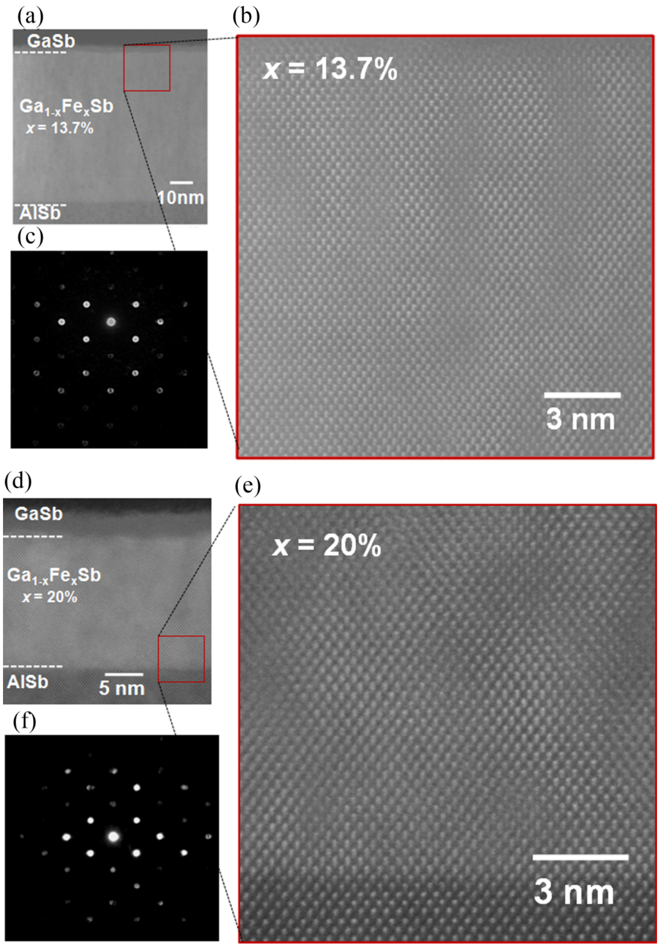

FIG. 2. (Color online) (a) Cross-sectional STEM image of the 100-nm-thick $(Ga_{1-x},Fe_x)Sb$ layer in sample E ($x = 13.7\%$). (b) High-resolution STEM image taken at an area marked by the red rectangle in (a). (c) TED of the $(Ga_{1-x},Fe_x)Sb$ layers in sample E ($x = 13.7\%$). (d) Cross-sectional STEM image of the 30-nm-thick $(Ga_{1-x},Fe_x)Sb$ layer in sample G ($x = 20\%$). (e) High-resolution STEM image taken at an area marked by the red rectangle in (d). (f) TED of the $(Ga_{1-x},Fe_x)Sb$ layer in sample G ($x = 20\%$). The STEM and TED patterns indicate that the crystal structure of samples E and G ($x = 13.7\%$ and 20%) is of zinc-blende type.

reference, we also show the RHEED pattern of an undoped GaSb sample grown at a high temperature (470 °C) in Fig. 1(b). The RHEED patterns of (Ga,Fe)Sb are streaky with weak surface reconstruction of (1 × 3), which is similar to that of GaSb. This suggests that these (Ga,Fe)Sb layers grown by LT-MBE maintain the zinc-blende crystal structure and have a nearly atomically smooth surface.

Figures 2(a) and 2(d) show the STEM lattice images of the two representative samples E and G ($x = 13.7\%$ and 20%) projected along the [110] axis, respectively. The upper (lower) interfaces between the (Ga,Fe)Sb layers and the GaSb cap (AlSb buffer) layers are nearly atomically smooth, consistent with the *in situ* RHEED observations. The magnified high-resolution STEM lattice images of areas indicated by red rectangles are shown in Figs. 2(b) and 2(e). In Figs. 2(c) and 2(f), we show the TED pattern of samples E and G, respectively. The STEM images and TED patterns indicate that the crystal structure of the (Ga,Fe)Sb layers is of zinc-blende type without any visible second phase such as metallic Fe, intermetallic Fe-Sb, or Fe-Ga precipitation. These results indicate that the epitaxial growth of zinc-blende $(Ga_{1-x},Fe_x)Sb$ is possible up to at least $x = 20\%$. At the same time, there are some contrast fluctuations in these STEM images, which may be related to the fluctuations of the local Fe concentration in the zinc-blende GaSb matrix. The influence of the fluctuations of the local Fe concentration on the ferromagnetism of (Ga,Fe)Sb layers will be discussed later.

B. Magneto-optical properties

We used reflection MCD spectroscopy to investigate the magneto-optical properties of (Ga,Fe)Sb. Here, the MCD intensity in reflection at a given photon energy is given by the difference between the reflectivity of right (R_{σ^+}) and left (R_{σ^-}) circular polarizations as follows: $\text{MCD} = \frac{90}{\pi}\frac{(R_{\sigma^+}-R_{\sigma^-})}{2R} \approx \frac{90}{\pi}\frac{1}{2R}\frac{dR}{dE}\Delta E$, where R is the reflectivity, E is the photon energy, and ΔE is the spin-splitting energy (Zeeman energy) of a material. Since the MCD spectrum shows the spin-polarized band structure of FMS and its magnitude is proportional to the magnetization, MCD is a very powerful method to judge whether a FMS is intrinsic or not [28]. Particularly, an intrinsic FMS layer shows a strong enhancement of the MCD intensity at their optical critical point energies, which reflect the spin-split band structure of the host semiconductor due to the s,p-d exchange interactions. In contrast, a nonmagnetic semiconductor layer containing metallic nanoclusters would show a broad MCD spectrum without any particular strong features of the semiconductor host, reflecting the metallic electronic structure of such nanoclusters [29]. For these reasons, we have employed the MCD characterizations in this paper.

1. $(\mathbf{Ga_{1-x},Fe_x})$Sb *samples* A–E *($x = 3.9\% - 13.7\%$)*

Figure 3 shows the MCD spectra of samples A–E ($x = 3.9\% - 13.7\%$) at 5 K with a magnetic field of 1 T applied perpendicular to the film plane. As a reference, we also show the MCD spectrum of an undoped GaSb, in which Zeeman splitting is very small. In contrast, the MCD spectra of (Ga,Fe)Sb show large Zeeman splitting with three strongly enhanced peaks at E_1 (2.19 eV), $E_1 + \Delta_1$(2.63 eV), and E_0' (3.19 eV) corresponding to the optical critical point energies of the GaSb band structure [30,31].This confirms that (Ga,Fe)Sb maintains the zinc-blende crystal structure with large spin-split band structure due to the s,p-d exchange interactions. At the same time, we observe no broad MCD background signal of the spectra, which would be observed if there were Fe-related metallic nanoclusters in the GaSb matrix. These MCD features are consistent with the TEM and TED results shown in Fig. 2. Next, we fitted Lorentzian curves to the MCD spectra near E_1 to determine the peak position of the E_1 optical transition energy. Figures 3(b) and 3(d) show the obtained values of E_1 as a function of x and lattice constant a. Figure 3(c) shows the intrinsic lattice constant a of the cubic zinc-blende type $(Ga_{1-x},Fe_x)Sb$ as a function of x, derived from the XRD spectra (see Ref. [27]) and corrected by taking into account the strain effect. The best fit to the data is given by the equation $a[\text{nm}] = 0.6091(1 - x) + 0.5918x$. The

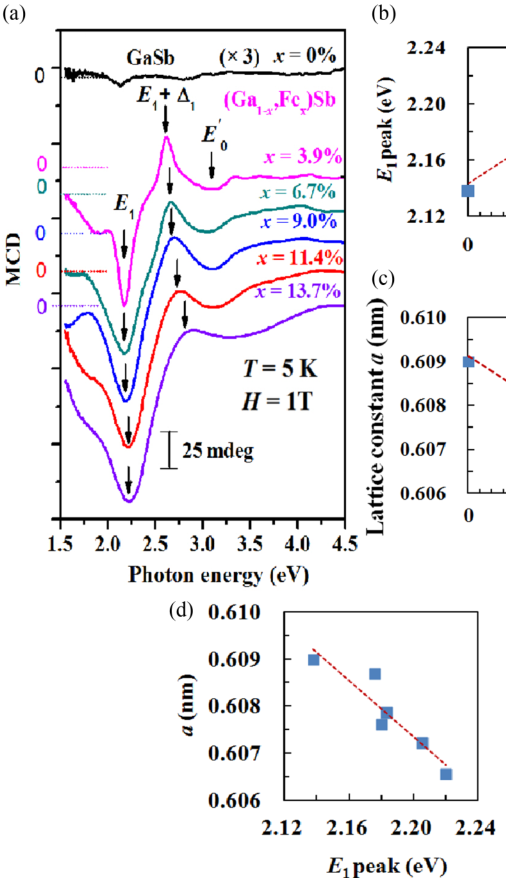

FIG. 3. (Color online) (a) Reflection MCD spectra measured at 5 K under a magnetic field of 1 T applied perpendicular to the film plane for $(Ga_{1-x},Fe_x)Sb$ samples A–E ($x = 3.9 - 13.7\%$). The MCD spectrum of a reference undoped GaSb sample is also shown. (b) Fe concentration x dependence of the E_1 transition energy of $(Ga_{1-x},Fe_x)Sb$ obtained from the MCD spectra. (c) Fe concentration (x) dependence of the lattice constant a of $(Ga_{1-x},Fe_x)Sb$. Here, a is the intrinsic lattice constant of the cubic zinc-blende type $(Ga_{1-x},Fe_x)Sb$, derived from the XRD spectra (Ref. [27]) and corrected by taking into account the strain effect. (d) Relationship between the lattice constant a of $(Ga_{1-x},Fe_x)Sb$ samples A–E ($x = 3.9 - 13.7\%$) and their E_1 transition energy.

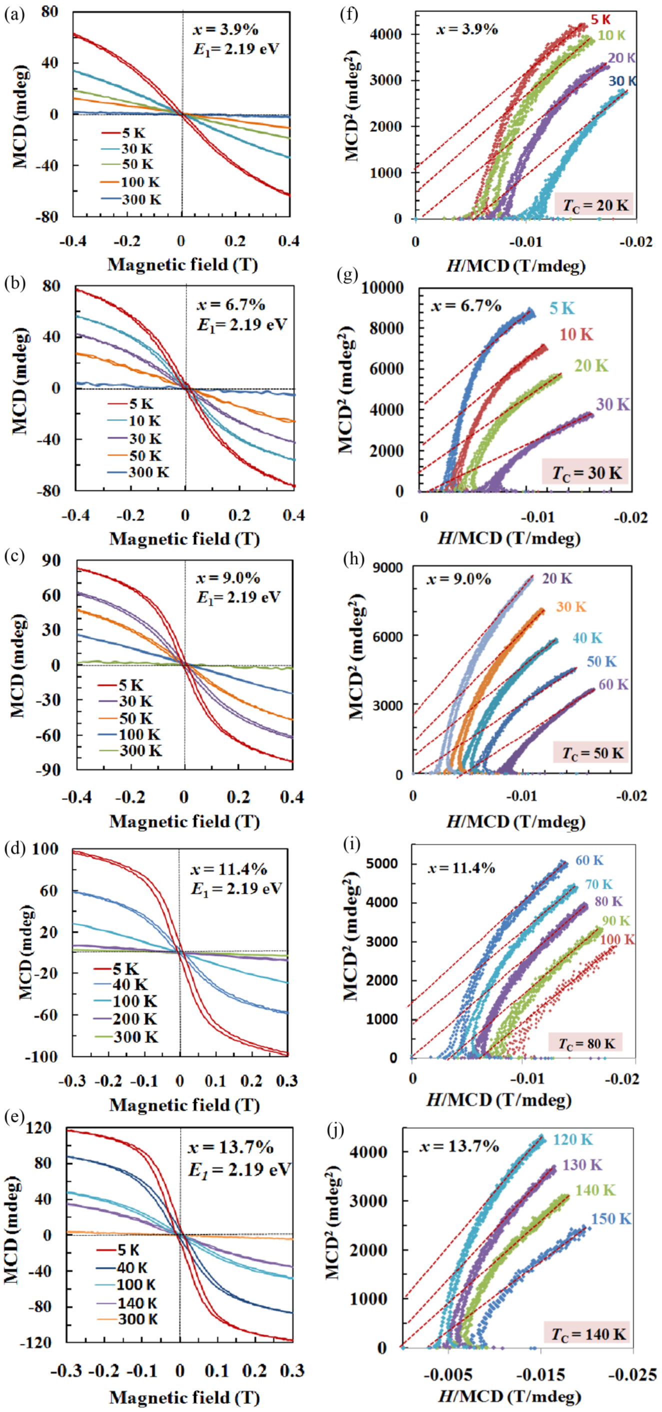

FIG. 4. (Color online) (a)–(e) MCD-H characteristics measured at a photon energy of 2.19 eV of 100-nm-thick (Ga,Fe)Sb samples A–E ($x = 3.9\% - 13.7\%$). (f)–(j) Corresponding Arrott plots of the MCD-H characteristics of samples A–E.

hypothetical zinc-blende FeSb lattice constant is 0.5918 nm, which is slightly higher than the previously estimated value of 0.5473 nm (see Ref. [27]) when ignoring the strain effect. One can see that the E_1 transition energy increases linearly from 2.14 eV to 2.22 eV as x increases from 0% to 13.7%. The blue shift of E_1 is consistent with the decrease of a, as shown in Fig. 3(d). Even more blue shifts can be seen for the $E_1 + \Delta_1$ and E'_0 peaks. These results confirm the successful growth of the zinc-blende (Ga,Fe)Sb alloy, whose lattice constant and band structure follow Vegard's law. It should be noted that the blue shift of E_1 has been also observed in an ellipsometric study of (Ga,Mn)As [32]. In (Ga,Mn)As, the lattice constant increases with Mn doping. Thus, the E_1 blue shift with increasing Mn doping cannot be explained simply by the change of the lattice constant. Instead, it is proposed that such a blue shift results from the hybridization between the Mn impurity band and the host GaAs valence band. The s and p bands of GaAs are repelled by the Mn d levels through the s,p-d hybridization, such that the d levels push the s,p band to lower energy [32].

Figures 4(a)–4(e) show the MCD-H characteristics of samples A–E ($x = 3.9\% - 13.7\%$) at different temperatures. Clear hysteresis curves were observed at low temperature, demonstrating the presence of ferromagnetic order at low temperature. At 300 K, MCD-H relationship becomes perfectly linear. Furthermore, the saturation MCD intensity decreases rapidly with increasing temperature. This two facts rule out the possibility of embedded Fe-related metallic nanoclusters such as Fe ($T_C = 1043$ K) or Fe $-$ Ga ($T_C = 393 - 1030$ K). Such Fe-related metallic nanoclusters, if they existed, would show Langevin-functionlike hysteresis in MCD-H characteristics at 300 K, and their saturation MCD intensity at high magnetic fields would be almost unchanged in the temperature range between 5–300 K. These results indicate that these samples do not contain superparamagnetic Fe-related metallic nanoclusters. Our results indicate that (Ga,Fe)Sb is an intrinsic FMS, containing no ferromagnetic Fe-related metallic nanoparticles. It should be also noted that other intermetallic Fe-Sb or Fe-Sb nanoclusters (if any) do not contribute to the ferromagnetism of the (Ga,Fe)Sb layers since none of such intermetallic Fe-Sb compounds are ferromagnetic; $Fe_{1+x}Sb$ is antiferromagnetic [33], and $FeSb_2$ is diamagnetic [34].

Figures 4(f)–4(j) show the corresponding Arrott plots of samples A–E. We found that T_C increases with x, consistent with the behavior of FMS. T_C is as high as 140 K for sample E ($x = 13.7\%$), despite the fact that GaSb is a narrow-gap semiconductor. Our result implies that the p-d exchange interaction is strong enough to induce ferromagnetism in (Ga,Fe)Sb, contrasting to the empirical trend predicted in Mn-based III-V FMSs, in which narrow gap Mn-based FMSs have much lower T_C [15,16].

2. (Ga_{1-x},Fe_x)Sb *samples* F_1-F_5 *($x = 17\%$, thickness* $d = 50 - 10$ nm*)*

In this section, we investigate the MCD spectra of a series of samples (F_1-F_5) with different thicknesses $d = 10-50$ nm while keeping the Fe concentration at $x = 17\%$. Figure 5(a) shows the MCD spectra of samples F_1-F_5, measured at 5 K. Figures 5(d) and 5(e) show the MCD-H characteristics and corresponding Arrott plots of the representative sample F_2 ($x = 17\%$ and $d = 40$ nm) at different temperatures. Clear observation of hysteresis at low temperature demonstrates ferromagnetic order in this sample.

T_C estimated by the Arrott plots of the MCD-H characteristics decreases from 180 K to 150 K with decreasing d (50–10 nm), as shown in Fig. 5(b), and is listed in the fourth column of Table I. This is consistent with the decrease of the saturation MCD intensity of the (Ga,Fe)Sb layers with decreasing d, as shown in Fig. 5(a). The reduction of T_C is probably due to the hole depletion in the (Ga,Fe)Sb layer. Such a depletion layer can exist at the interfaces between the AlSb buffer/(Ga,Fe)Sb and the (GaFe)Sb/GaSb cap/surface. As the (Ga,Fe)Sb layer becomes thinner than 40 nm, the effect of the depletion layer becomes more significant. As a result, the averaged hole concentration decreases and leads to lower T_C [we will show later that T_C of (Ga,Fe)Sb depends on the Fe concentration x and hole concentration p approximately as $x\,p^{1/3}$]. Moreover, we observed a blue shift of the E_1 transition energy as d decreases, as shown in Fig. 5(b). To understand this behavior, we plot the blue shift of the E_1 transition energy ($E_1 - E_{1,\mathrm{bulk}}$) as a function of the total thickness L of the (Ga,Fe)Sb and GaSb cap layers, as shown Fig. 5(c). Here, we assumed that $E_{1,\mathrm{bulk}}$ is the same as the E_1 peak energy of the 50-nm-thick sample. The relationship between ($E_1 - E_{1,\mathrm{bulk}}$) and L seems to follow $E_1 - E_{1,\mathrm{bulk}} = cL^{-2}$, where c is a constant (as shown by the dashed curve in Fig. 5(c)), suggesting that the blue shift of the E_1 energy in MCD spectra is probably due to the quantum size effect in the AlSb/(GaFeSb/GaSb)/surface quantum well. Note that the band offset at the L point of AlSb/GaSb is 0.31 eV [35,36]; thus, the AlSb and surface are the potential barriers, while the (GaFeSb/GaSb) double layers (which include the depleted layers on both sides) constitute the quantum well. Such a blue shift of the peak E_1 due to the quantum size effect has been recently clearly observed in quantum wells with an (In,Fe)As layer [24,37].

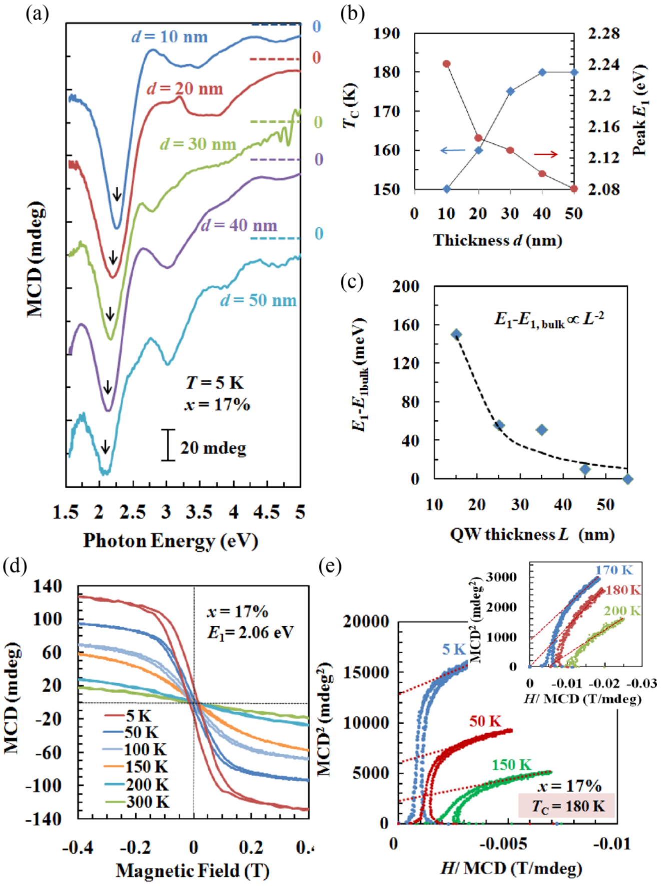

FIG. 5. (Color online) (a) Reflection MCD spectra measured at 5 K under a magnetic field of 1 T applied perpendicular to the film plane for samples F_1-F_5 ($x = 17\%$, thickness $d = 50 - 10$ nm). (b) d dependence of T_C (blue diamonds) and E_1 (red circles). (c) Blue shift of E_1 transition energy ($E_1 - E_{1,\mathrm{bulk}}$) plotted as a function of the total thickness L of (Ga,Fe)Sb/GaSb cap layer. Here, we assumed that $E_{1,\mathrm{bulk}}$ is the same as the E_1 peak energy of the 50-nm-thick sample. (d) MCD-H characteristics measured at E_1 of the (Ga_{1-x},Fe_x)Sb samples F_2 ($x = 17\%$, $d = 40$ nm) at various temperatures (5–300 K). (e) Corresponding Arrott plots of the MCD-H characteristics in (d).

3. *Heavily Fe-doped* (Ga_{1-x},Fe_x)Sb *sample* G *($x = 20\%$)*

We then investigate the magneto-optical properties of a 30-nm-thick heavily Fe-doped (Ga_{1-x},Fe_x)Sb sample with $x = 20\%$ (sample G). Since the crystal quality of the thin

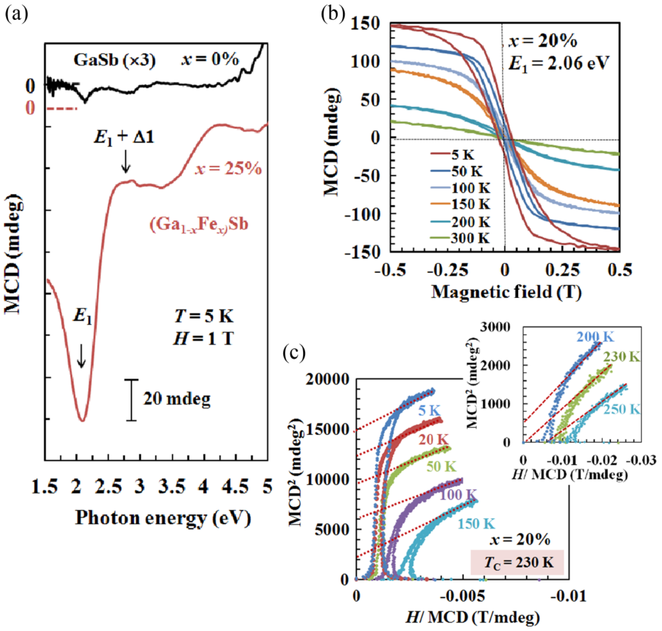

FIG. 6. (Color online) (a) Reflection MCD spectra measured at 5 K under a magnetic field of 1 T applied perpendicular to the film plane for the heavily Fe-doped $(Ga_{1-x},Fe_x)Sb$ sample G ($x = 20\%$). The MCD spectrum of a reference undoped GaSb sample is also shown. (b) MCD-H characteristics measured at E_1 of $(Ga_{1-x},Fe_x)Sb$ sample G ($x = 20\%$) at various temperatures (5–300 K). (c) Corresponding Arrott plots of the MCD-H characteristics in (b).

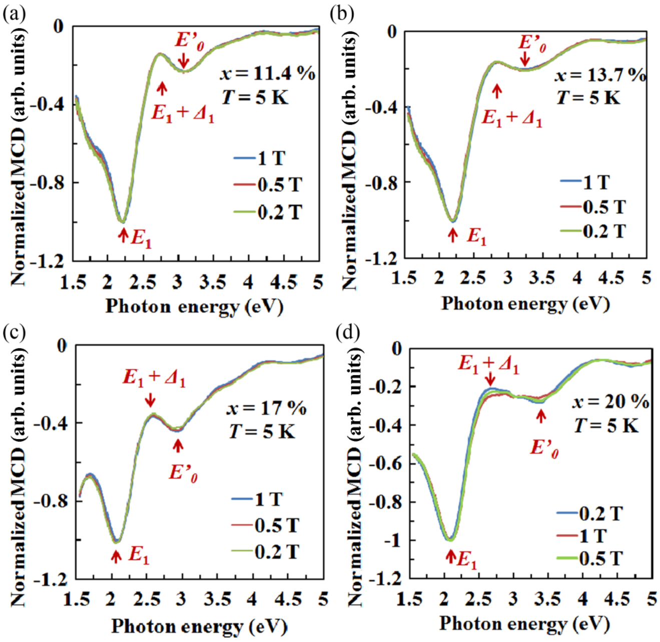

FIG. 7. (Color online) (a)–(d) Normalized MCD spectra of $(Ga_{1-x},Fe_x)Sb$ samples D, E, F_2, and G ($x = 11.4 - 20\%$) measured at 5 K under various magnetic field of $H = 0.2$, 0.5, and 1 T. Here, the MCD intensity at each photon energy is normalized by the one at E_1.

films with high x is often better than that of the thick films, the thickness of the $(Ga_{1-x},Fe_x)Sb$ film ($x = 20\%$) was reduced to 30 nm to keep good crystal quality and to prevent phase separation. We first recall that despite heavy Fe doping, this sample preserves the zinc-blende crystal structure, as shown in the STEM images and TED pattern in Figs. 2(d)–2(f). Figure 6(a) shows the MCD spectrum of sample G at 5 K with a magnetic field of 1 T applied perpendicular to the film plane. The MCD spectrum shows strongly enhanced peaks as compared with that of an undoped GaSb, indicating the large spin-split band structure due to the s,p-d exchange interactions. However, unlike samples A–E, whose E_1 peaks show blue shift due to the reduced lattice constant, the E_1 peak of sample G (2.09 eV) shows a slight red shift as compared with that of undoped GaSb (2.14 eV). We found that this was accompanied by a sudden increase of the lattice constant, which was confirmed by our XRD measurement. The reason for this behavior is unclear at this stage. However, it may be similar to the red shift discussed in (Ga,Mn)As [32], resulting from the band-gap renormalization due to the ionized donor impurities (As antisite As_{Ga}). In the heavily Fe-doped sample $(Ga_{1-x},Fe_x)Sb$ ($x = 20\%$), the ionized impurities increase due to the increase of acceptor defects. Thus, the red shift caused by the band-gap renormalization due to the impurities may overcome the blue shift caused by the decrease of the lattice constant and/or the s,p-d hybridization. As a result, the red shift of E_1 can be observed in this heavily Fe-doped $(Ga_{1-x},Fe_x)Sb$ sample with $x = 20\%$.

Nevertheless, the MCD spectrum preserves the features of the GaSb band structure, indicating that this particular heavily Fe-doped (Ga,Fe)Sb sample also maintains the zinc-blende crystal and band structure. Figures 6(b) and 6(c) show the MCD-H characteristics and corresponding Arrott plots of sample G at various temperatures. T_C of sample G ($x = 20\%$) is as high as 230 K, which is the highest value so far reported in III-V FMSs.

4. *Normalized MCD spectra and MCD-H characteristics*

In the following, we analyze the normalized MCD spectra and MCD-H characteristics of samples D, E ($x = 11.4\%$, 13.7%, $d = 100$ nm), F_2 ($x = 17\%$, $d = 40$ nm), and G ($x = 20\%$, $d = 30$ nm), which show relatively high T_C, in order to characterize their ferromagnetism in more details. Figures 7(a)–7(d) show the normalized MCD spectra by their intensity at E_1 of these four samples, measured at 5 K with an applied magnetic field of 0.2, 0.5, and 1 T. The normalized MCD spectra of samples D–F_2($x = 11.4\% - 17\%$) show nearly perfect overlapping on a single spectrum in the whole photon-energy range, indicating that the MCD spectra come from a single phase ferromagnetism of the entire (Ga,Fe)Sb film. This overlapping can also be seen in their normalized MCD-H characteristics measured at different photon energies (E_1, $E_1 + \Delta_1$, and E'_0) shown in Figs. 8(a)–8(c). However, the normalized MCD spectra of sample G ($x = 20\%$) deviates slightly from a single spectrum at photon energies 2.5–3.5 eV [see Fig. 7(d)]. The normalized MCD-H characteristics of sample G measured at different photon energies also show a little deviation at E_1 (2.09 eV). Nevertheless, all the normalized MCD spectra of sample G preserves the spectral features of zinc-blende GaSb, as shown in Fig. 7(d), a fact that is consistent with the observed STEM images and TED pattern. The slight deviation of the normalized magneto-

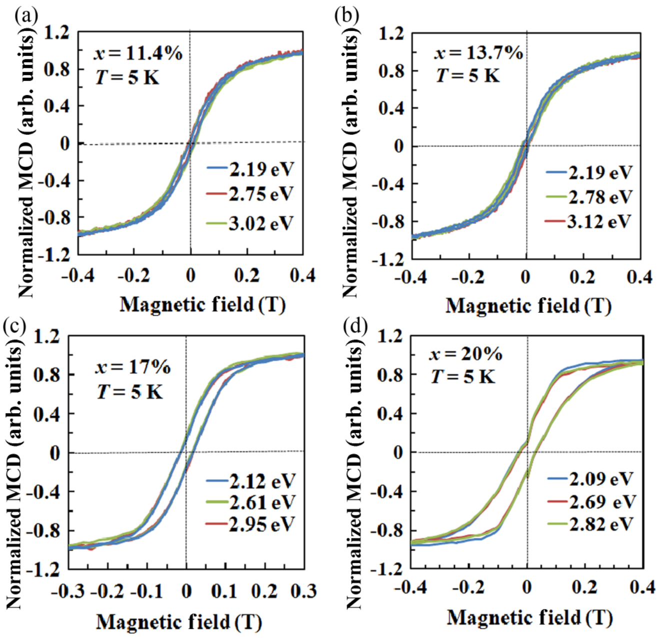

FIG. 8. (Color online) (a)–(d) Normalized MCD-H characteristics of $(\mathrm{Ga}_{1-x},\mathrm{Fe}_x)\mathrm{Sb}$ samples D–G ($x = 11.4 - 20\%$) measured at various photon energies. Here, the MCD intensity at each magnetic field is normalized by the one at 1 T.

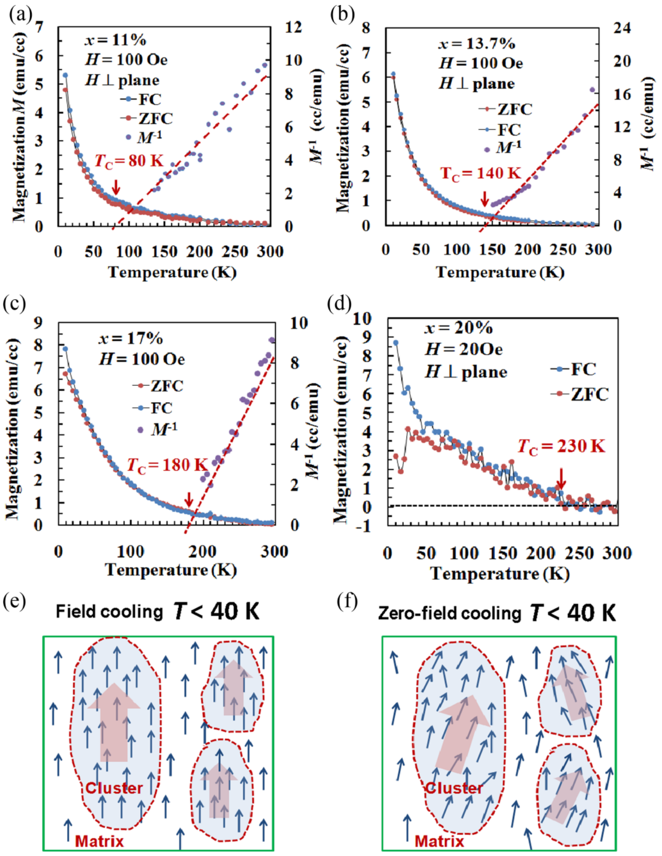

FIG. 9. (Color online) (a)–(d) Temperature dependence of the magnetization ($M-T$ curves) of samples D, E, F$_2$, and G ($x = 11.4 - 20\%$) measured by SQUID. The samples were cooled from room temperature to 10 K under two conditions; with a magnetic field of 1 T (FC, blue dots) and zero magnetic field (ZFC, red dots). After cooling, the magnetization was measured with increasing temperature with a weak magnetic field of 20–100 Oe applied perpendicular to the plane along the GaAs [001] direction. In Figs. 9(a)–9(c), the purple dots show the inverse FC magnetization (M^{-1}) at high temperature, which follows the Curie-Weiss law. (e), (f) Schematic pictures of magnetic states in (Ga,Fe)Sb sample G ($x = 20\%$) at $T < 40$ K in the field cooling and zero field cooling process, respectively. Here, small blue arrows express the magnetic moments of Fe atoms, nanoscale clusters are illustrated by light-blue areas surrounded by red dashed curves, and the total magnetic moments of these clusters are expressed by big pink arrows.

optical characteristics of this particular sample G can be explained by the local fluctuation of the Fe concentration in the zinc-blende GaSb matrix due to spinodal decomposition. Such spinodal decomposition typically results in two phases [38,39]. One is the zinc-blende (Ga,Fe)Sb matrix phase, and the other is the superparamagnetic zinc-blende (Ga,Fe)Sb clusters with higher Fe concentration. The nanoscale dark contrasts in the STEM image shown Fig. 2(e) may be attributed to such high Fe concentration areas. Due to the difference in atomic number Z of (Ga,Fe)Sb alloy components ($Z_{\mathrm{Ga}} = 31$, $Z_{\mathrm{Sb}} = 51$, $Z_{\mathrm{Fe}} = 26$), the STEM image of (Ga,Fe)Sb areas with high Fe concentration would appear darker than those of (Ga,Fe)Sb areas with lower Fe concentration. The shape of the MCD spectrum of these two phases must be slightly different in the range of $2.5 - 3.5$ eV, since the positions of peaks $E_1 + \Delta_1 (\approx 2.6\,\mathrm{eV})$ and $E_0' (\approx 2.9\,\mathrm{eV})$ depend on the Fe concentration, as shown in Fig. 3. At the same time, the two phases can have different responses to the magnetic field, as the superparamagnetic nanoscale clusters are unconnected and should have softer hysteresis than the ferromagnetic matrix phase. These explain the slight deviation of the normalized MCD spectra and MCD-H characteristics. The local fluctuation of the Fe concentration will be further investigated by SQUID measurements in the following section.

C. Magnetization

Next, we further investigate the magnetic properties of (Ga,Fe)Sb by SQUID measurements. Four samples D, E, F$_2$, and G ($x = 11.4 - 20\%$) were cooled from room temperature to 10 K under two conditions, with a magnetic field of 1 T perpendicular to the film plane [field cooling (FC)] and zero magnetic field [zero field cooling (ZFC)]. After cooling, the magnetization was measured while increasing temperature with a magnetic field of 100 Oe (or 20 Oe) applied perpendicular to the film plane. Figures 9(a)–9(d) show the FC (blue) and ZFC (red) magnetization versus temperature ($M-T$) curves of samples D, E, F$_2$, and G. The $M-T$ curves of samples D–F$_2$ ($x = 11.4 - 17\%$) show nearly the same monotonic behavior for both ZFC and FC, supporting single phase ferromagnetism in these samples. In contrast, the $M-T$ curve of sample G ($x = 20\%$) shows a separation between FC and ZFC at 40 K, suggesting the existence of superparamagnetic zinc-blende (Ga,Fe)Sb nanoclusters with high Fe concentrations. This result is consistent with the normalized MCD spectra and MCD-H characteristics and the observation of the clusterlike contrast in the STEM image. The magnetic states in sample G at a temperature lower than 40 K in the FC and ZFC processes are illustrated in Figs. 9(e) and 9(f). The magnetic moments of Fe atoms are illustrated by small blue arrows. Due to the local fluctuation of the Fe concentration, zinc-blend clusters with high Fe concentration are formed. The total magnetic moments of those clusters are expressed by big pink arrows. The superparamagnetic behavior appears due to the existence of such unconnected nanoscale clusters shown by light-blue areas surrounded by red dashed curves. The nonuniform Fe distribution in sample G is a natural result of the spinodal decomposition phenomena at high doping concentration, similar to the cases of many other FMSs such as GaMnAs [40], ZnCrTe [41], and GeFe [42].

We then estimate T_C of these (Ga,Fe)Sb samples from the $M-T$ curves. For samples D–F$_2$ ($x = 11.4 - 17\%$), which have small remanent magnetization, a magnetic field of 100 Oe was applied to obtain clear signals. Therefore, we estimate T_C of these samples by the Curie-Weiss plot at high temperatures. In Figs. 9(a)–9(c), the purple dots show the inverse of the FC magnetization (M^{-1}) under a magnetic field of 100 Oe at high temperatures, which follows the Curie-Weiss law. The T_C values estimated from the Curie-Weiss plots are 80 K, 140 K, and 180 K for samples D, E, and F$_2$ ($x = 11.4\%$, 13.7%, and 17%), respectively, which are exactly the same as those estimated by the Arrott plots of their MCD-H hystereses. For sample G ($x = 20\%$), which has larger magnetization, a smaller magnetic field of 20 Oe was applied, and T_C was estimated directly by the disappearance of M in the $M-T$ curve, as shown in Fig. 9(d). The estimated T_C of $\sim$230 K for sample G ($x = 20\%$) is in good agreement with that estimated by the Arrott plots of its MCD-H characteristics [see Fig. 6(c)].

Figure 10(a) shows the $M-H$ curves of samples D, E, F$_2$, and G ($x = 11.4 - 20\%$) at 5 K when the magnetic field was applied perpendicular to the film plane. The saturation magnetization, remanent magnetization, and coercive force increase systematically with increasing x. The averaged magnetic moment per Fe atom at saturation of samples D, E, F$_2$, and G are estimated to be about $2.4 - 2.9\,\mu_B$ per doped Fe atom and are listed in the eighth column of Table I. These values are close to the theoretical value calculated in Fe-doped GaSb by linear muffin-tin orbital tight binding (LMTO-TB) method ($2.28\,\mu_B$) [43] and larger than those of Fe atoms ($2.2\,\mu_B$) in Fe metal and Mn atoms ($1.5 - 2.2\,\mu_B$) in (Ga,Mn)As [44]. Figure 10(b) shows the $M-H$ curves of sample G ($x = 20\%$) measured at 5 K with a magnetic field applied in the film plane along the [110] axis and perpendicular to the film plane along the [001] axis. One can see that the perpendicular magnetization saturates around 0.5 T, while the in-plane magnetization saturates around 0.8 T. Furthermore, the perpendicular remanent magnetization and coercive force are larger than those in plane. Thus, this result suggests that the perpendicular axis is the easy axis of magnetization.

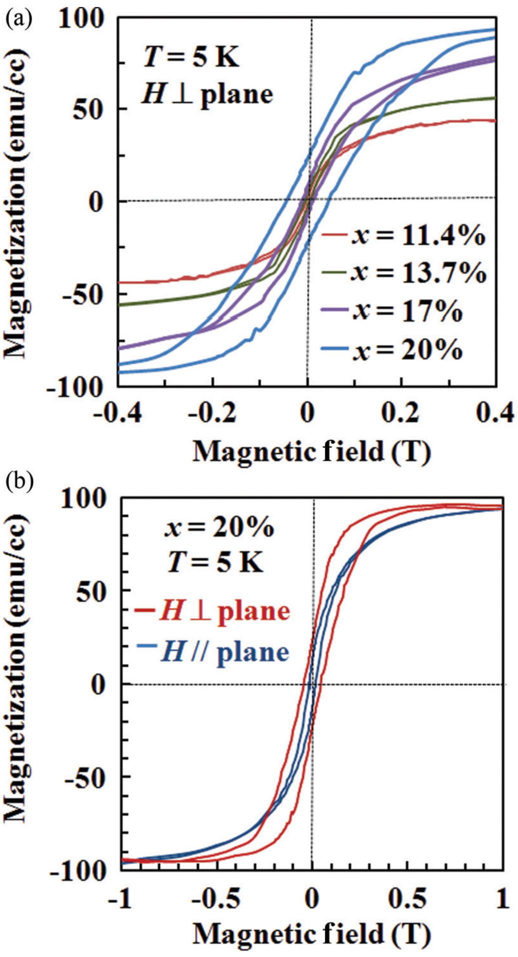

FIG. 10. (Color online) (a) Magnetization hysteresis curves ($M-H$) of samples D, E, F$_2$, and G ($x = 11.4 - 20\%$) measured at 5 K. (b) $M-H$ curves of sample G ($x = 20\%$) measured at 5 K when the magnetic field was applied in plane along the [110] axis (blue curve) and perpendicular to the plane (red curve).

D. Magnetotransport properties

Next, we investigate the magnetotransport properties of the (Ga,Fe)Sb samples. The resistivity ρ and hole concentration p, which is approximately estimated by Hall effect data measured at 300 K, are listed in the fifth and sixth columns of Table I. For the samples with relatively low T_C($x \leqslant 13.7\%$, $T_C \leqslant 140$ K), we assume that the contribution of the AHE at 300 K is small and can be neglected. For the samples with relatively high T_C ($x \geqslant 17\%$), we cannot estimate the hole concentration due to the influence of the AHE even at 300 K. As shown in the sixth column of Table I, p increases from 4.4×10^{18} to $4.6 \times 10^{19}\ \mathrm{cm}^{-3}$ as x increases. This result may be explained by the increase of native acceptor defects due to the Fe doping, such as antisite Ga. Figures 11(a)–11(d) show the Hall resistance versus magnetic field (R_{Hall}-H) characteristics at various temperatures of samples D, E, F$_2$, and G ($x = 11.4 - 20\%$) (for the sample with $x = 11.4\%$, we cannot measure the Hall effect at 5 K due to its high resistance). At low temperatures, R_{Hall} is dominated by the AHE with clear hysteresis, which is consistent with the MCD-H characteristics.

In order to understand the mechanism of AHE in (Ga,Fe)Sb, we plotted the anomalous Hall conductivity σ_{xy} of samples D, E, F$_2$, and G ($x = 11.4 - 20\%$) as a function of conductivity σ_{xx} [see Fig. 11(e)] with vertical and horizontal axes in the logarithmic scale. Assuming that the ordinary Hall effect is small at low temperatures, the anomalous Hall conductivity σ_{xy} is estimated by $\sigma_{xy} = \frac{\rho_{xy}}{\rho_{xy}^2+\rho_{xx}^2}$, and the conductivity σ_{xx} is given by $\sigma_{xx} = \frac{\rho_{xx}}{\rho_{xx}^2+\rho_{xy}^2}$. Here, ρ_{xx} and ρ_{xy} are the resistivity and anomalous Hall resistivity, respectively. It has been known

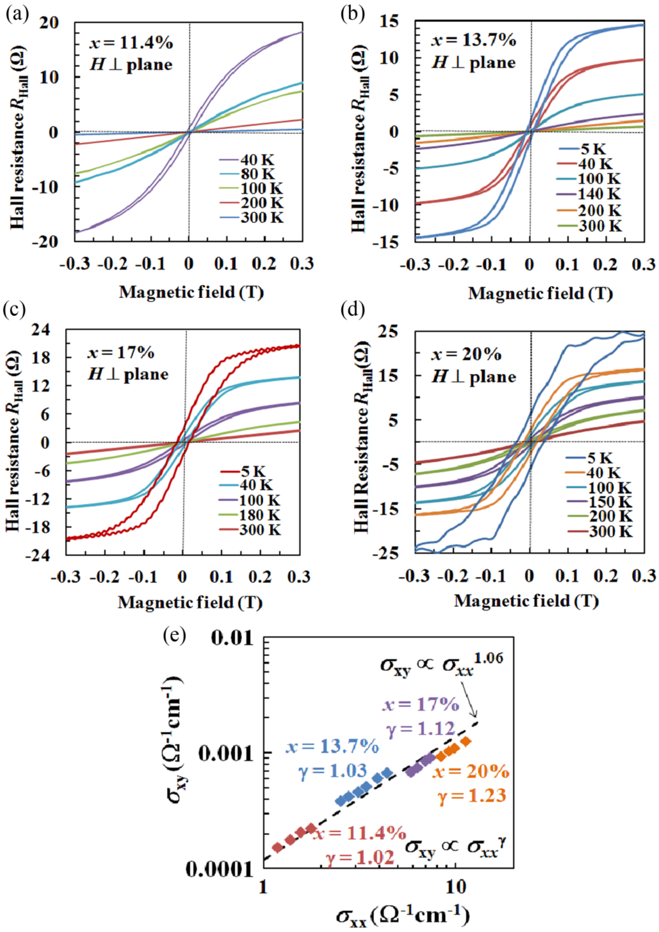

FIG. 11. (Color online) (a)–(d) Hall resistance R_{Hall} versus magnetic field H measured at various temperatures of samples D, E, F_2, and G ($x = 11.4-20\%$). (e) The relationship between the anomalous Hall conductivity σ_{xy} and conductivity σ_{xx} of samples D, E, F_2, and G ($x = 11.4-20\%$). The dashed line shows the fitting line with $\sigma_{xy} \propto \sigma_{xx}^{1.06}$.

that there is a relation $\sigma_{xy} \propto \sigma_{xx}^{\gamma}$, with γ depending on the mechanism of AHE. The black dashed line in Fig. 11(e) shows the fitting $\sigma_{xy} \propto \sigma_{xx}^{1.06}$. One can see that γ is approximately equal to 1, indicating that AHE in (Ga,Fe)Sb is governed by the skew-scattering mechanism.

Figures 12(a)–12(d) show the corresponding Arrott plots of the R_{Hall}-H characteristics at various temperatures. The T_C values estimated by the Arrott plots of R_{Hall}-H and MCD-H characteristics are in good agreement, thus supporting the intrinsic ferromagnetism of (Ga,Fe)Sb. At 300 K, the R_{Hall}-H characteristics are linear with positive slopes, indicating that all samples are p-type.

Next, we examined the magnetoresistance (MR) to investigate the spin-dependent scattering in our (Ga,Fe)Sb samples. Figures 13(a)–13(d) show the MR curves of samples D, E, F_2, and G ($x = 11.4-20\%$), measured at different temperatures with an external magnetic field applied perpendicular to the film plane. Clear hystereses in the MR curves were observed at $T < T_C$ and disappeared at $T > T_C$. All MR curves show negative MR. Here, we attempt to explain the observed negative MR in (Ga,Fe)Sb by the spin disorder scattering theory [45]. In this theory, when a magnetic field is applied, the spin dependent scattering is reduced due to the alignment of localized magnetic moments along the magnetic field direction. As a result, the resistivity decreases with increasing the magnetic field. We employ the following semi-empirical formula proposed by Khosla and Fischer [46] to fit to the experimental data,

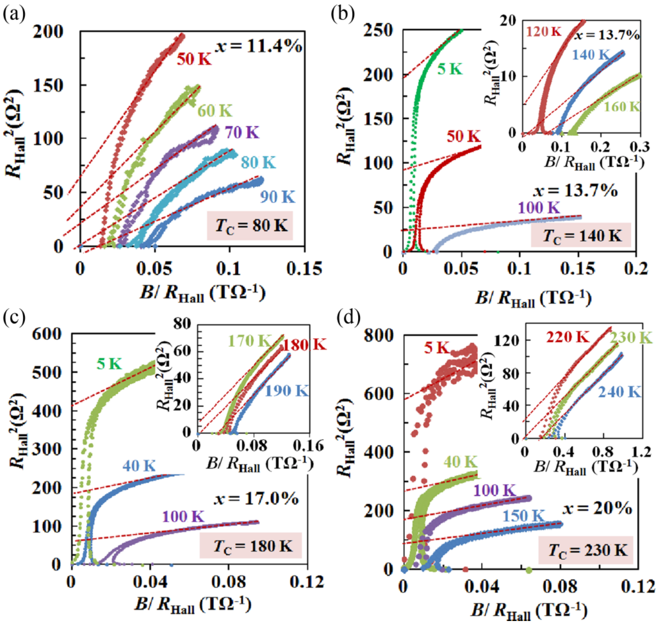

FIG. 12. (Color online) (a)–(d) Arrott plots of the R_{Hall}-H characteristics of samples D–G ($x = 11.4-20\%$).

$$\frac{\Delta\rho}{\rho} = -B_1^2 \ln\left(1 + B_2^2 H^2\right). \tag{1}$$

Here, H is the applied magnetic field. The parameters B_1 and B_2, which include the physical characteristics of the exchange interaction, are given by

$$B_1 = A_1 J D(E_F)[S(S+1) + \langle M^2 \rangle], \tag{2}$$

$$B_2^2 = \left[1 + 4S^2\pi^2\left(\frac{2JD(E_F)}{g}\right)^4\right]\left(\frac{g\mu_B}{\alpha k_B T}\right)^2, \tag{3}$$

where J is the exchange interaction energy, g is the Lan factor, $D(E_F)$ is the density of states at the Fermi energy, $\langle M \rangle$ is the average magnetization, T is temperature, α is a numerical factor that is on the order of unity, and S is the total spin of the localized magnetic moment. A_1 is the parameter of spin scattering contribution to the total MR. Figure 13(e) shows the representative fittings using Eq. (1) to the MR curves of samples D, E, F_2, and G ($x = 11.4-20\%$) measured at 200 K. Here, the measurement temperature is higher than T_C of samples D–F_2 ($x = 11.4-17\%$) and close to that ($T_C \sim 230$ K) of sample G ($x = 20\%$); thus, the effect of remanent magnetization on the MR curves is zero or small and can be negligible. The colored and black lines in Fig. 13(e) are the experimental data and fitting results using Eq. (1), respectively. The fittings reproduce the observed MR data quite well for all the samples, indicating that spin disorder scattering is the origin of the observed negative MR. The negative MR

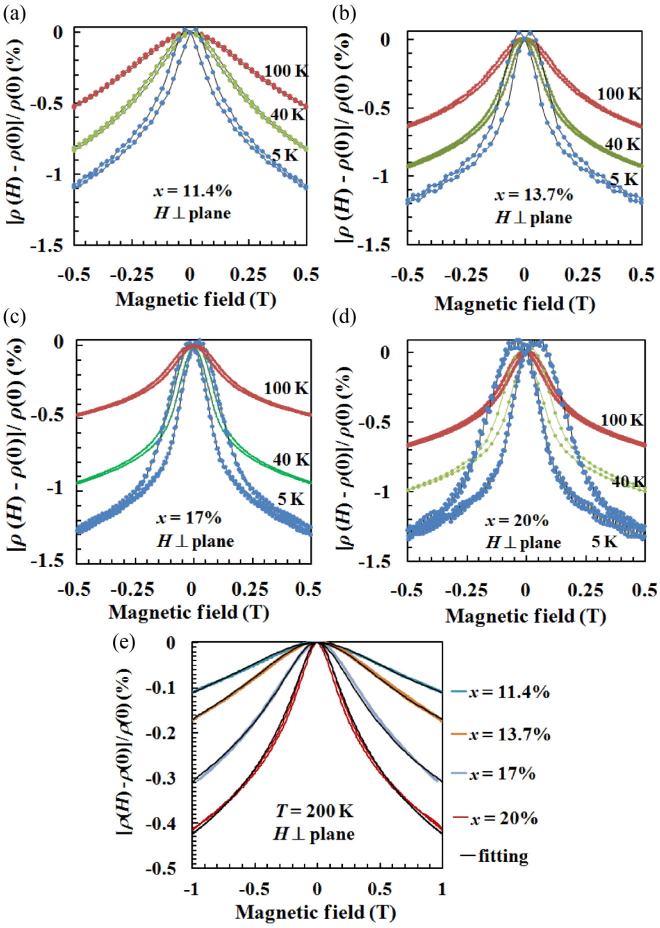

FIG. 13. (Color online) (a)–(d) Magnetoresistance (MR) $[\rho(H) - \rho(0)]/\rho(0)$ as a function of applied magnetic field H for four samples D, E, F_2, and G ($x = 11.4 - 20\%$) at different temperatures. The magnetic field was applied perpendicular to the film plane. (e) MR for four samples with D, E, F_2, and G ($x = 11.4 - 20\%$) at 200 K. Colored curves are experimental data, and black curves are fittings using the Khosla and Fisher's formula (Ref. [46]).

TABLE II. Magnetoresistance (MR) ratio of $(Ga_{1-x},Fe_x)Sb$ samples D, E, F_2, and G ($x = 11.4 - 20\%$) at 200 K and fitting parameters obtained by fitting Eq. (1) to the experimental MR curves. The MR ratio is defined as $[\rho(0.95\,T) - \rho(0)]/\rho(0)$, where $\rho(H)$ is the resistivity at a magnetic field of H.

Sample	x(%)	MR (%)	B_1	$B_2(T^{-1})$
D	11.4	−0.10	0.068	4.5
E	13.7	−0.15	0.091	6.0
F_2	17	−0.31	0.099	22.5
G	20	−0.41	0.110	50

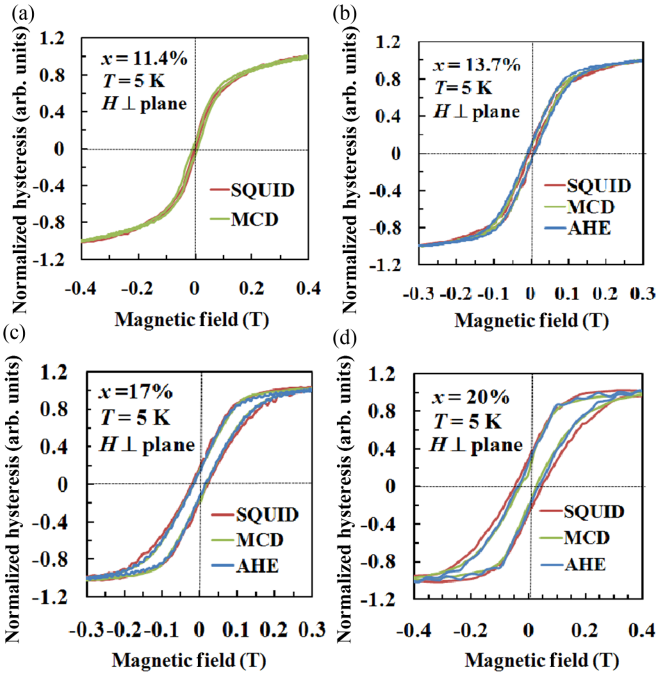

FIG. 14. (Color online) (a) Comparison of the normalized magnetic field dependences of MCD, magnetization, and AHE measured at 5 K for samples D–G ($x = 11.4 - 20\%$). For the sample with $x = 11.4\%$, AHE can be not measured at 5 K due to its high resistance.

ratio, defined as $[\rho(0.95\,T) - \rho(0)]/\rho(0)$, where $\rho(H)$ is the resistivity at a magnetic field of H, and the fitting parameters B_1 and B_2 at 200 K obtained from the fittings by Eq. (1) are listed in the third through fifth columns of Table II. One can see that B_1 and B_2 increase with increasing x, and B_2 increases much more strongly than B_1. The change ratio of B_2 is roughly equal to square of that of B_1. The change of B_1 and B_2 are consistent with the prediction of Eqs. (2) and (3), in which B_1 and B_2 are proportional to $D(E_F)$ and $D(E_F)^2$, respectively. Although Fe atoms do not directly supply carriers, acceptor defects such as antisite Ga can be increased with increasing x. As a result, the hole density [hence the density of states $D(E_F)$] is increased with increasing x. The observed negative MR induced by spin-scattering is similar to the cases of other FMSs such as (In,Mn)As [47] or (In,Mn)Sb [48], thus further supporting the intrinsic ferromagnetism in (Ga,Fe)Sb.

E. Comparison between SQUID, AHE, and MCD

Here, we show normalized hysteresis curves (magnetic field dependences) of samples D, E, F_2, and G ($x = 11.4 - 20\%$) measured by SQUID, AHE, and MCD at 5 K (for the sample with $x = 11.4\%$, we cannot measure AHE at 5 K due to its high resistance). For samples D−F_2 ($x = 11.4 - 17\%$), hysteresis curves measured by different methods perfectly agree with each other [see Figs. 14(a)–14(c)], indicating the single ferromagnetic phase in these samples. Meanwhile, the normalized $M-H$ curve of sample G ($x = 20\%$) is slightly different from the normalized R_{Hall}-H and MCD-H curves. This deviation can also be explained by the two ferromagnetic (Ga,Fe)Sb phases in sample G; one is the matrix phase and the other is the cluster phase with high Fe concentrations, both of which are of zinc-blende crystal structure. Since the relative fraction of contribution of each phase to the total magnetization, magnetotransport, and magneto-optical properties can be different, it is not surprising that the hysteresis curves measured by different methods are slightly different from each other for the particular sample G.

IV. DISCUSSION

The observation of high T_C up to 230 K in (Ga,Fe)Sb is striking because extensive studies on Mn-based FMSs over the past 15 years have been done based on the theoretical prediction [15,16] that T_C decreases with decreasing the semiconductor bandgap. Even for the intermediate bandgap (Ga,Mn)As, the highest T_C is limited to 200 K. Thus, important questions that must be addressed here are (1) whether the observed ferromagnetism in (Ga,Fe)Sb is intrinsic or not, and (2) if intrinsic, determining what the mechanism for such strong ferromagnetism is.

In this paper, we have presented systematic and comprehensive studies on the crystal structure, magneto-optical properties, magnetization, and magnetotransport properties of various $(Ga_{1-x},Fe_x)Sb$ samples. All of the data indicate that $(Ga_{1-x},Fe_x)Sb$ maintains the zinc-blende crystal structure and is an intrinsic FMS, although there is local Fe concentration fluctuation for the most heavily Fe-doped sample with $x = 20\%$. In the following, we summarize the results that support intrinsic ferromagnetism while ruling out other extrinsic origins due to second-phase ferromagnetic precipitations in (Ga,Fe)Sb.

(i) The *in situ* RHEED observation, STEM lattice images, and TED patterns show the zinc-blende crystal structure of (Ga,Fe)Sb without any other second phase of precipitations. The (Ga,Fe)Sb surfaces and interfaces are nearly atomically flat.

(ii) The lattice constant of (Ga,Fe)Sb estimated by XRD follows Vegard's law.

(iii) The MCD spectra shows strongly enhanced features at the optical critical point energies E_1 (2.19 eV), $E_1 + \Delta_1$ (2.63 eV), and E_0' (3.19 eV) of GaSb.

(iv) There is no broad background signal in the MCD spectra that would be observed if there were Fe-related metallic precipitations.

(v) The peak energy E_1 in the MCD spectra shows blue shift with increasing the Fe concentration x and decreasing the lattice constant.

(vi) The temperature dependence of the MCD-H hysteresis and saturated MCD intensity cannot be explained by high-T_C superparamagnetic precipitations.

(vii) T_C is not a constant but increases with increasing x.

(viii) For a fixed x, T_C decreases with decreasing the layer thickness d of (Ga,Fe)Sb, which is explained by the hole depletion effect in semiconducting (Ga,Fe)Sb.

(ix) For a fixed x, the peak E_1 shows blue shift with decreasing the total layer thickness L of (Ga,Fe)Sb/GaSb double layers as $1/L^2$, which is explained by the quantum size effect in (Ga,Fe)Sb/GaSb quantum wells.

(x) T_C values estimated by the SQUID measurements agree with those estimated by the Arrott plots of MCD-H and R_{Hall}-H hysteresis.

(xi) The observed negative MR follows the Khosla and Fischer theory of spin-disorder scattering due to local magnetic moments.

(xii) The normalized magnetization hysteresis curves measured by MCD, SQUID, and AHE coincide with each other except for heavily doped sample G, which shows spinodal decomposition.

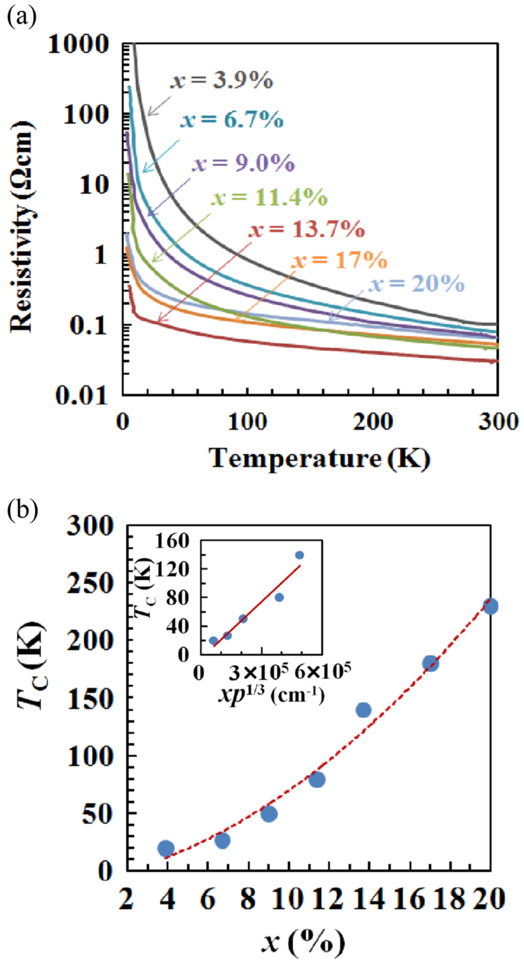

FIG. 15. (Color online) (a) Temperature dependence of the electrical resistivity for samples A–E, F_2, and G ($x = 3.9\% - 20\%$). (b) Fe concentration x dependence of T_C. Inset shows T_C versus $xp^{1/3}$.

All of these features support the intrinsic ferromagnetism in (Ga,Fe)Sb. The remaining question is the mechanism for such strong ferromagnetism despite the fact that the host material GaSb is a narrow-gap semiconductor. To answer this question, we first show that the ferromagnetism in (Ga,Fe)Sb also depends on the hole concentration, as in the case of other p-type FMSs with hole-induced ferromagnetism. Note that the first hint of hole-induced ferromagnetism was given by feature (viii), in which T_C decreases with decreasing the layer thickness d of (Ga,Fe)Sb, which can be naturally explained by the hole depletion effect combined with the hole-induced ferromagnetism.

In Fig. 15(a), we show the temperature dependence of the electrical resistivity ρ of samples A–E, F_2, and G ($x = 3.9 - 20\%$). The resistivity was measured in the temperature range from 5 to 300 K. One can see that ρ decreases as x increases due to the increase of the hole concentration. Samples A–C ($x \leqslant 9\%$) show insulating behavior, while samples D, E, F_2, and G ($x \geqslant 11.4\%$) show nearly metallic behavior; ρ is nearly constant at $T > 10$ K. These results show that the more metallic the sample is, the higher T_C it has. This is similar to the trend observed in (Ga,Mn)As. Figure 15(b) shows the T_C values of all samples plotted as a function of x. One can see that T_C increases as x increases. However, T_C is not linearly proportional to x. Instead, T_C is approximately proportional to $xp^{1/3}$, as shown in the inset of Fig. 15(b). This indicates that T_C also depends on p, as in the case of hole-induced ferromagnetism.

Next, we attempt to use the *p-d* Zener model to estimate the strength of the *p-d* exchange interaction in (Ga,Fe)Sb. Although it is not clear whether the mechanism of hole-induced ferromagnetism in (Ga,Fe)Sb is given by the *p-d* Zener model or not, an estimation of an effective *p-d* exchange interaction using this model will help us make a comparison with Mn-doped FMSs. According to the mean-field *p-d* Zener model [15,16], T_C is given by the following equation: $T_\mathrm{C} = xN_0S(S+1)\beta^2A_\mathrm{F}D(E_\mathrm{F})/12k_\mathrm{B}$. Here, N_0 is the concentration of cation sites, β is the *p-d* the exchange integral, k_B is Boltzmann's constant, $S = 5/2$ is the Fe local spin, A_F is the Fermi liquid parameter, and $D(E_\mathrm{F})$ is the density of states at the Fermi energy. We use the hole concentration data of samples A–E ($x = 3.9\% - 13.7\%$) to estimate $N_0\beta$. (The *p-d* exchange interaction of the samples with $x = 17\%$ and 20% cannot be estimated since the hole concentration p cannot be obtained for these samples because of the strong AHE contribution to the Hall effect data.) We assume that the effective mass values of light holes and heavy holes in (Ga,Fe)Sb are the same as those of GaSb and $A_\mathrm{F} = 1$. The exchange interaction $N_0\beta$ is estimated to be about 1.6–1.9 eV, as listed in the seventh column of Table I. These values are larger than the *p-d* exchange interaction reported for (Ga,Mn)As ($N_0\beta = 1.2$ eV). Therefore, T_C of (Ga,Fe)Sb with $x = 13.7\%$ (sample E) reaches 140 K even when p is as low as $4.6 \times 10^{19}\ \mathrm{cm}^{-3}$, while T_C of the same value in Mn-doped FMSs often requires a much higher hole concentration of $10^{20} \sim 10^{21}\ \mathrm{cm}^{-3}$. Using these values, T_C up to 300 K is expected for a (Ga,Fe)Sb sample with $x = 13.7\%$ and $p = 5 \times 10^{20}\ \mathrm{cm}^{-3}$, indicating that (Ga,Fe)Sb is a promising material for realizing room temperature ferromagnetism in FMS.

Figure 16(a) shows the highest T_C values of various III–V FMSs reported so far. Here, we plot the T_C values of bulklike III–V films (not including the results of Mn δ-doping [49] and zinc-blende MnAs nanostructures [40,50]). T_C of Mn-doped III–V FMSs (green circles) tends to be lower with narrowing the band gap of the host semiconductor. In contrast, inverse behavior is observed in Fe-doped III–V FMSs (red diamonds); T_C tends to be higher with narrowing the band gap. To explain this behavior, we have proposed a resonant *s,p-d* exchange interaction model in Fe-based narrow gap FMSs [22,24], in which the *d* level of Fe (ε_d) lies near the conduction band bottom (E_C) of InAs, as shown in Fig. 16(b), and these close ε_d and E_C enhance T_C. The band lineup of host semiconductors was taken from Refs. [51] and [52]. It has been known that the *s,p-d* exchange interaction energy is given by the Anderson Hamiltonian [53,54],

$$N_0\alpha \text{ or } N_0\beta = -2\left|V_{s,p\text{-}d}\right|^2\left(\frac{1}{E_{\mathrm{C,V}}-\varepsilon_\mathrm{d}}+\frac{1}{U-E_{\mathrm{C,V}}+\varepsilon_\mathrm{d}}\right). \tag{4}$$

Here, N_0 is the density of cation sites, α and β are the *s,p-d* exchange integral, $E_\mathrm{C,V}$ is the energy at the bottom of the conduction band (the top of the valence band), ε_d is the energy level of *d* states, U is the Coulomb repulsion between opposite-spin electrons in a *d* state, and $V_{s,p\text{-}d}$ is the *s,p-d* mixing potential. Therefore, the *s-d* exchange interaction in (In,Fe)As can be large when $E_\mathrm{C} - \varepsilon_\mathrm{d}$ is small [55]. Furthermore, according to the vacuum pining rule [56,57], the *d* level of transition metal atoms weakly depends on their semiconductor hosts, and the *d* level of Fe should lie near the top of the valence band (E_V) of GaSb. Also, the theoretical calculation of the electronic structure of Fe-doped GaSb by the spin-polarized LMTO-TB method also indicates that the Fe *d* level is at the top of the GaSb valence band [43]. As a result, (Ga,Fe)Sb has a large *p-d* exchange interaction and high Curie temperature. On the other hand, (Ga,Fe)As is a paramagnetic semiconductor [58] because the *d* level of Fe is in the band gap; thus, the *s,p-d* exchange interaction in (Ga,Fe)As is too small to induce ferromagnetism.

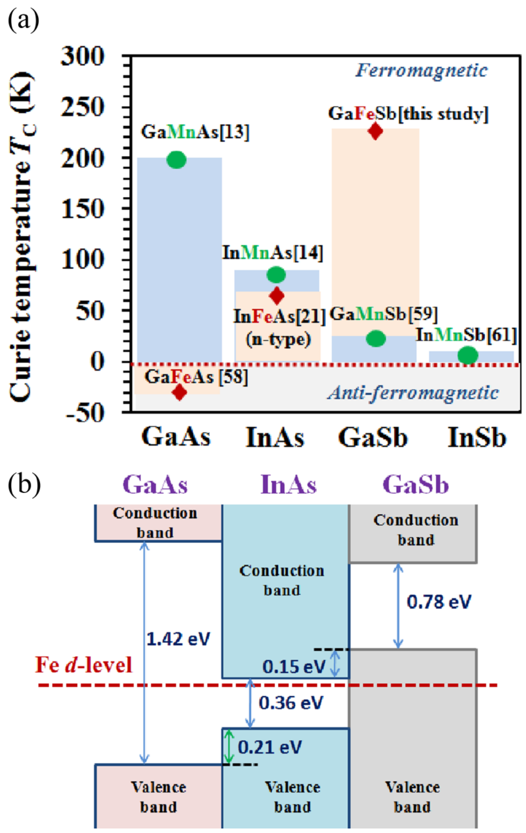

FIG. 16. (Color online) (a) Highest T_C values reported so far in Mn-doped (green circles) and Fe-doped (red diamonds) III–V FMSs. T_C of the Mn-δ-doped GaAs [49] and zinc-blende MnAs nanostructures [40,50] are not included. (b) Band structure alignment of InAs, GaAs, and GaSb and the position of the Fe *d*-level (dashed line).

V. CONCLUSION

In conclusion, *p*-type FMSs $(\mathrm{Ga}_{1-x},\mathrm{Fe}_x)\mathrm{Sb}$ ($x = 3.9 - 20\%$) thin films were successfully grown by LT-MBE and show intrinsic ferromagnetism. The obtained T_C (230 K) of (Ga,Fe)Sb ($x = 20\%$) is the highest in III–V FMSs, indicating that T_C of Fe-doped III–V FMSs tends to be higher in narrow gap semiconductors, in contrast to the trend observed in Mn-doped FMSs. The obtained T_C (230 K) of (Ga,Fe)Sb ($x = 20\%$) is much higher than that of (Ga,Mn)Sb ($T_C = 25$ K) [59], (In,Mn)Sb ($T_C = 10$ K) [61], (In,Mn)As ($T_C = 90$ K) [14], and even (Ga,Mn)As ($T_C = 200$ K) [13]. These results suggest that the position of the *d* level of the transition metals in the host semiconductor band structure plays an important role to induce ferromagnetism [60]. Our results demonstrate that Fe-based FMSs are promising for semiconductor spintronic devices as well as requiring revision of the current understanding of ferromagnetism in FMSs.

ACKNOWLEDGMENTS

This paper is supported by Grant-in-Aids for Scientific Research, including the Specially Promoted Research, and the Project for Developing Innovation Systems of MEXT. Part of this paper was carried out under the Cooperative Research Project Program of RIEC, Tohoku University. P.N.H acknowledges support from the Yazaki Memorial Foundation for Science and Technology, the Murata Science Foundation, and the Toray Science Foundation. L.D.A. acknowledges support from the JSPS Fellowship for Young Scientists (KAKENHI Grant No. 257388) and the Program for Leading Graduate Schools (MERIT).

---

[1] H. Ohno, J. Magn. Magn. Mater. **200**, 110 (1999).

[2] T. Jungwirth, Jairo Sinova, J. Mašek, J. Kučera, and A. H. MacDonald, Rev. Mod. Phys. **78**, 809 (2006).

[3] M. Tanaka, S. Ohya, and P. N. Hai, Appl. Phys. Rev. **1**, 011102 (2014).

[4] M. Kohda, Y.Ohno, K. Takamura, F. Matsukura, and H. Ohno, Jpn. J. Appl. Phys. **40**, L1274 (2001).

[5] S. Sugahara and M. Tanaka, Appl. Phys. Lett. **84**, 2307 (2004).

[6] S. Sugahara and M. Tanaka, J. Appl. Phys. **97**, 10D503 (2005).

[7] M. Tanaka and S. Sugahara, IEEE Trans. Electron Devices **54**, 961 (2007).

[8] H. Munekata, H. Ohno, S. von Molnar, A. Segmüller, L. L. Chang, and L. Esaki, Phys. Rev. Lett. **63**, 1849 (1989).

[9] S. Koshihara, A. Oiwa, M. Hirasawa, S. Katsumoto, Y. Iye, C. Urano, H. Takagi, and H. Munekata, Phys. Rev. Lett. **78**, 4617 (1997).

[10] H. Ohno, A. Shen, F. Matsukura, A. Oiwa, A. Endo, S. Katsumoto, and Y. Iye, Appl. Phys. Lett. **69**, 363 (1996).

[11] Hayashi, M. Tanaka, T. Nishinaga, H. Shimada, H. Tsuchiya, and Y. Otuka, J. Cryst. Growth **175–176**, 1063 (1997).

[12] Ohno, D. Chiba, F. Matsukura, T. Omiya, E. Abe, T. Dietl, Y. Ohno, and K. Ohtani, Nature **408**, 944 (2000).

[13] L. Chen, X. Yang, F. Yang, J. Zhao, J. Misuraca, P. Xiong, and S. von Molnar, Nano Lett. **11**, 2584 (2011).

[14] T. Schallenberg and H. Munekata, Appl. Phys. Lett. **89**, 042507 (2006).

[15] T. Dietl, H. Ohno, F. Matsukura, J. Cibert, and D. Ferrand, Science **287**, 1019 (2000).

[16] T. Dietl, H. Ohno, and F. Matsukura, Phys. Rev. B **63**, 195205 (2001).

[17] K. S. Burch, D. B. Shrekenhamer, E. J. Singley, J. Stephens, B. L. Sheu, R. K. Kawakami, P. Schiffer, N. Samarth, D. D. Awschalom, and D. N. Basov, Phys. Rev. Lett. **97**, 087208 (2006).

[18] S. Ohya, K. Takata, and M. Tanaka, Nat. Phys. **7**, 342 (2011).

[19] S. Ohya, I. Muneta, Y. Xin, K. Takata, and M. Tanaka: Phys. Rev. B **86**, 094418 (2012).

[20] M. Dobrowolska, K. Tivakornsasithorn, X. Liu, J. K. Furdyna, M. Berciu, K. M. Yu, and W. Walukiewicz, Nat. Mater. **11**, 444 (2012).

[21] P. N. Hai, L. D. Anh, S. Mohan, T. Tamegai, M. Kodzuka, T. Ohkubo, K. Hono, and M. Tanaka, Appl. Phys. Lett. **101**, 182403 (2012).

[22] P. N. Hai, L. D. Anh, and M. Tanaka, Appl. Phys. Lett. **101**, 252410 (2012).

[23] P. N. Hai, D. Sasaki, L. D. Anh, and M. Tanaka, Appl. Phys. Lett. **100**, 262409 (2012).

[24] L. D. Anh, P. N. Hai, and M. Tanaka, Appl. Phys. Lett. **104**, 042404 (2014).

[25] A. Twardowski, P. Świderski, M. von Ortenberg, and R. Pauthenet, Solid State Commun. **50**, 509 (1984).

[26] J. Okabayashi, A. Kimura, O. Rader, T. Mizokawa, A. Fujimori, T. Hayashi, and M. Tanaka, Phys. Rev. B **58**, R4211 (1998).

[27] N. T. Tu, P. N. Hai, L. D. Anh, and M. Tanaka, Appl. Phys. Lett. **105**, 132402 (2014).

[28] K. Ando and H. Munekata, J. Magn. Magn. Mater. **272–276**, 2004 (2004).

[29] H. Shimizu and M. Tanaka, J. Appl. Phys. **89**, 7281 (2001).

[30] R. R. L. Zucca and Y. R. Shen, Phys. Rev. B **1**, 2668 (1970).

[31] D. E. Aspnes, C. G. Olson, and D. W. Lynch, Phys. Rev. B **14**, 4450 (1976).

[32] K. S. Burch, J. Stephens, R. K. Kawakami, D. D. Awschalom, and D. N. Basov, Phys. Rev. B **70**, 205208 (2004).

[33] K. Yamaguchi, H. Yamamoto, Y. Yamaguchi, and H. Watanabe, J. Phys. Soc. Jpn. **33**, 1292 (1972).

[34] P. Sun, N. Oeschler, S. Johnsen, B. B. Iversen, and F. Steglich, Appl. Phys. Express **2**, 091102 (2009).

[35] A. A. Kopylov, Solid State Commun. **56**, 1 (1985).

[36] J. R. Chelikowski and M. L. Cohen, Phys. Rev. B **14**, 556 (1976).

[37] D. Sasaki, L. D. Anh, P. N. Hai, and M. Tanaka, Appl. Phys. Lett. **104**, 142406 (2014).

[38] K. Sato, H. Katayama-Yoshida, and P. H. Dederichs, Jpn. J. Appl. Phys., Part 2 **44**, L948 (2005).

[39] P. N. Hai, S. Yada, and M. Tanaka, J. Appl. Phys. **109**, 073919 (2011).

[40] M. Yokoyama, H. Yamaguchi, T. Ogawa, and M. Tanaka, J. Appl. Phys. **97**, 10D317 (2005).

[41] S. Kuroda, N. Nishizawa, K. Takita, M. Mitome, Y. Bando, K. Osuch, and T. Dietl, Nat. Mater. **6**, 440 (2007).

[42] Y. Shuto, M. Tanaka, and S. Sugahara, Appl. Phys. Lett. **90**, 132512 (2007).

[43] V. A. Gubanov, C. Y. Fong, and C. Boekema, Phys. Stat. Sol. (b) **218**, 599 (2000).

[44] P. A. Korzhavyi, I. A. Abrikosov, E. A. Smirnova, L. Bergqvist, P. Mohn, R. Mathieu, P. Svedlindh, J. Sadowski, E. I. Isaev,

Yu. Kh. Vekilov, and O. Eriksson, Phys. Rev. Lett. **88**, 187202 (2002)

[45] Y. Toyozawa, J. Phys. Soc. Jpn. **17**, 986 (1962).

[46] R. P. Khosla and J. R. Fischer, Phys. Rev. B **2**, 4084 (1970).

[47] S. J. May, A. J. Blattner, and B. W. Wessels, Phys. Rev. B **70**, 073303 (2004).

[48] J. A. Peters, N. D. Parashar, N. Rangaraju, and B. W. Wessels, Phys. Rev. B **82**, 205207 (2010).

[49] A. M. Nazmul, T. Amemiya, Y. Shuto, S. Sugahara, and M. Tanaka, Phys. Rev. Lett. **95**, 017201 (2005).

[50] M. Moreno, A. Trampert, B. Jenichen, L. Däweritz, and K. H. Ploog, J. Appl. Phys. **92**, 4672 (2002).

[51] H. Kroemer, Physica E **20**, 196 (2004).

[52] J. Brubach, A. Yu. Silov, J. E. M. Haverkort, W. v. d. Vleuten, and J. H. Wolter, Phys. Rev. B **59**, 10315 (1999).

[53] P. W. Anderson, Phys. Rev. **124**, 41 (1964).

[54] J. R. Schrieffer and P. A. Wolff, Phys. Rev. **149**, 491 (1966).

[55] M. Kobayashi (private communication). The bandstructure of (In,Fe)As characterized by angle-resolved photoemission spectroscopy is consistent with the picture described here.

[56] L. A. Ledebo and B. K. Ridley, J. Phys. C: Solid State Phys. **15**, L961 (1982).

[57] M. J. Caldas, A. Fazzio, and Alex Zunger, Appl. Phys. Lett. **45**, 671 (1984).

[58] S. Haneda, M. Yamaura, Y. Takatani, K. Hara, S. Harigae, and H. Munekata, Jpn. J. Appl. Phys. **39**, L9 (2000).

[59] E. Abe, F. Matsukura, H. Yasuda, Y. Ohno, and H. Ohno, Physica E **7**, 981 (2000).

[60] N. T. Tu, L. D. Anh, P. N. Hai, and M. Tanaka, Jpn. J. Appl. Phys. **53**, 04EM05 (2014).

[61] K. Ganesan and H. L. Brat, J. Appl. Phys. **103**, 043701 (2008).